Cooperative Near-IR to Visible Photon Upconversion in Yb^{3+}-Doped $MnCl_2$ and $MnBr_2$: Comparison with a Series of Yb^{3+}-Doped Mn^{2+} Halides

Pascal Gerner, Christine Reinhard, and Hans U. Güdel*[a]

Abstract: Yb^{3+}-doped $MnCl_2$ and $MnBr_2$ crystals exhibit strong red upconversion luminescence under near-infrared excitation around 10000 cm^{-1} at temperatures below 100 K. The broad red luminescence band is centred around 15200 cm^{-1} for both compounds and identified as the Mn^{2+} $^4T_{1g} \rightarrow {}^6A_{1g}$ transition. Excitation with 10 ns pulses indicates that the upconversion process consists of a sequence of ground-state and excited-state absorption steps. The experimental VIS/NIR photon ratio at 12 K for an excitation power of 191 mW focused on the sample with a 53 mm lens is 4.1 % for $MnCl_2$:Yb^{3+} and 1.2 % for $MnBr_2$:Yb^{3+}. An upconversion mechanism based on exchange coupled Yb^{3+}–Mn^{2+} ions is proposed. Similar upconversion properties have been reported for $RbMnCl_3$:Yb^{3+}, $CsMnCl_3$:Yb^{3+}, $CsMnBr_3$:Yb^{3+}, $RbMnBr_3$:Yb^{3+}, Rb_2MnCl_4:Yb^{3+}. The efficiency of the upconversion process in these compounds is strongly dependent on the connectivity between the Yb^{3+} and Mn^{2+} ions. The VIS/NIR photon ratio decreases by three orders of magnitude along the series of corner-sharing Yb^{3+}-Cl^--Mn^{2+}, edge-sharing Yb^{3+}-$(Cl^-)_2$-Mn^{2+} to face-sharing Yb^{3+}-$(Br^-)_3$-Mn^{2+} bridging geometry. This trend is discussed in terms of the dependence of the relevant superexchange pathways on the Yb^{3+}–Mn^{2+} bridging geometry.

Keywords: exchange interaction · laser spectroscopy · luminescence · upconversion

Introduction

Photon upconversion (UC) provides an efficient way to convert long wavelength radiation into shorter wavelength light.[1,2] In contrast to second harmonic generation or two photon absorption processes, UC requires at least two metastable excited states, and UC luminescence can also be excited with non-coherent input radiation. Many of the rare earth (RE) ions provide multiple metastable excited states, and UC research has been mainly devoted to lanthanide and actinide doped crystals and glasses. UC phenomena in transition metal (TM) ion doped crystals are rare. A number of observations involving 3d, 4d and 5d TM ions have been reported and analysed in recent years.[2–5] A variety of UC mechanisms have been suggested, and several technical applications have been achieved since UC was reported by Auzel in 1966.[6,7]

In our research we have extended the UC investigations to mixed RE/TM systems. This turned out to be an almost unexplored but very fertile field, and various new phenomena have been reported.[8–11] Using chemical variation with the aim of tuning the light emission properties is a major part of our research strategy. Mixed RE/TM systems are of interest in this context, as the TM excited states are more susceptible to chemical and structural changes in the ligand environment than RE excited states.

A few years ago we discovered visible (VIS) Mn^{2+} $^4T_{1g} \rightarrow {}^6A_{1g}$ luminescence in Yb^{3+} doped $RbMnCl_3$ crystals at cryogenic temperatures after laser excitation into sharp line Yb^{3+} $^2F_{7/2} \rightarrow {}^2F_{5/2}$ absorptions in the near-IR (NIR) around 1 μm.[12] This most unusual phenomenon was without precedent at the time, and the experimental data were interpreted on the basis of exchange coupling between adjacent Yb^{3+} and Mn^{2+} ions in the lattice. Exchange interactions between ions in insulating materials are not only dependent on the distance but also on the bridging geometry between the coupled ions. These first results led to a systematic study of Yb^{3+}-doped Mn^{2+} halides with specific bridging geometries between Yb^{3+} and Mn^{2+} ions. Yb^{3+} substitutes for Mn^{2+} with concomitant charge compensation in all halides studied. Thus there are three possible connections of adjacent Yb^{3+} and Mn^{2+} ions via halide bridges: corner-sharing, edge-sharing and face-sharing. With the exception of the edge-sharing case we have studied several examples, involving the other bridging geometries: $RbMnCl_3$:Yb^{3+}[12] (corner-sharing and face-sharing), $CsMnCl_3$:Yb^{3+}[13] (corner-sharing), Rb_2MnCl_4:Yb^{3+}[14] (corner-sharing), $RbMnBr_3$:Yb^{3+}[15] (face-sharing), $CsMnBr_3$:Yb^{3+}[16] (face-

[a] P. Gerner, Dr. C. Reinhard, Prof. Dr. H. U. Güdel
Departement für Chemie und Biochemie
Freiestrasse 3, 3000 Bern 9 (Switzerland)
Fax: (+41) 31-631-43-99
E-mail: hans-ulrich.guedel@iac.unibe.ch

 DOI: 10.1002/chem.200400282

sharing). In the present study we complement the systematics by studying the two edge-sharing systems $MnCl_2$:Yb^{3+} and $MnBr_2$:Yb^{3+}. The results of these two systems are then put into the context of the existing data. A correlation between the efficiency of the UC process and the bridging geometry is established and interpreted in terms of very simple considerations about exchange interactions in an Yb^{3+}–Mn^{2+} dimer.

Results

In Figure 1a the 12 K Yb^{3+} luminescence excitation spectrum of $MnCl_2$:0.1 % Yb^{3+} monitored at 9823 cm^{-1} (see full arrow in Figure 1d) is shown. The dominant sharp line Yb^{3+} excitation features at 10179 and 10765 cm^{-1} are assigned to the Yb^{3+} $^2F_{7/2}\rightarrow{}^2F_{5/2}$ absorption transitions. The less intense features around 10359 cm^{-1} are attributed to Yb^{3+} vibronic intensity. On the right side in Figure 1b the relevant part of the axial absorption spectrum of $MnCl_2$:0.1 % Yb^{3+} at 12 K is shown. The bands centred at 18450, 21900 and 23580 cm^{-1} are due to the Mn^{2+} $^6A_{1g}\rightarrow{}^4T_{1g}$, $^4T_{2g}$, $^4A_{1g}/{}^4E_g$ absorption transitions, respectively.[17] Figure 1d shows the 12 K unpolarized survey luminescence spectrum (upside down) after laser excitation into the dominant Yb^{3+} $^2F_{7/2}\rightarrow{}^2F_{5/2}$ absorption feature at 10765 cm^{-1} (see full arrow in Figure 1c). Three distinct luminescence band systems are observed. Band I in the near-infrared (NIR) corresponds to the Yb^{3+} $^2F_{5/2}\rightarrow{}^2F_{7/2}$ luminescence. The broad band II centred in the red spectral region around 15000 cm^{-1} is assigned to Mn^{2+} $^4T_{1g}\rightarrow{}^6A_{1g}$ UC luminescence (see also Figure 2a). The weak sharp line features of band III around 19660 cm^{-1} are ascribed to a cooperative Yb^{3+} pair luminescence.[16] The asterisk denotes a peak due to stray light of the frequency doubled Nd^{3+}/YVO_4 laser used to pump the Ti/sapphire NIR source. Note the different scaling factors for the luminescence bands II and III compared with band I in Figure 1d. In Figure 1c the 12 K excitation spectrum of the Mn^{2+} luminescence at 15384 cm^{-1} (see dashed arrow in Figure 1d) in the Yb^{3+} absorption region is presented. It closely follows the Yb^{3+} excitation spectrum in Figure 1a, and the same Yb^{3+} absorption transitions are observed in both spectra.

For $MnBr_2$:0.06 % Yb^{3+} (data not shown) the dominant Yb^{3+} $^2F_{7/2}\rightarrow{}^2F_{5/2}$ excitation features are located at 10079 and 10675 cm^{-1}. The Mn^{2+} $^4T_{1g}$, $^4T_{2g}$, $^4A_{1g}/{}^4E_g$ absorption bands are centred at 18330, 21600 and 23100 cm^{-1}, respectively. And the luminescence behaviour with bands I, II and III is similar to $MnCl_2$:0.1 % Yb^{3+}.

In Figure 2 the upper part shows the Mn^{2+} $^4T_{1g}$ luminescence of $MnCl_2$:Yb^{3+} after Yb^{3+} excitation at 10765 cm^{-1} (a) and direct Mn^{2+} $^4T_{2g}$ excitation at 21838 cm^{-1} (b) at 12 K. For NIR excitation the Mn^{2+} $^4T_{1g}$ luminescence is centred at 15240 cm^{-1} (a) and red shifted by 210 cm^{-1} compared with the direct Mn^{2+} excitation (b). The lower part of Figure 2 shows the corresponding data for $MnBr_2$:Yb^{3+} at 12 K. In this case the red shift upon NIR excitation is 80 cm^{-1}. The insets show a double logarithmic representation of the red UC luminescence intensity as a function of the laser power for $MnCl_2$:Yb^{3+} and $MnBr_2$:Yb^{3+} after 12 K excitation at 10765 cm^{-1} (c) and at 10675 cm^{-1} (f), respectively. Linear fits to the low power region up to 25 mW yield slopes of 1.86 in c) and 2.02 in f).

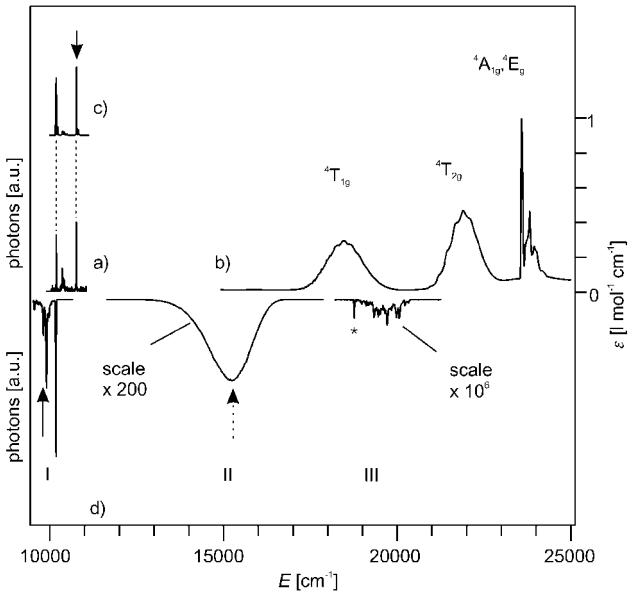

Figure 1. Data for $MnCl_2$:Yb^{3+} a) 12 K excitation spectrum of the Yb^{3+} luminescence monitored at 9823 cm^{-1} (full arrow in d). b) Axial Mn^{2+} absorption spectrum at 12 K. c) 12 K excitation spectrum of the Mn^{2+} luminescence monitored at 15380 cm^{-1} (dashed arrow in d). d) Overview luminescence spectrum after direct Yb^{3+} $^2F_{7/2}\rightarrow{}^2F_{5/2}$ laser excitation at 10765 cm^{-1} at 12 K (full arrow in c). Note the scaling factors for the different emissions. The asterisk (*) denotes a peak due to stray light of the 532 nm pump source.

Figure 3 shows the temporal evolution of the 12 K Mn^{2+} $^4T_{1g}$ luminescence intensity in $MnCl_2$:Yb^{3+} monitored at 15380 cm^{-1} after 10 ns excitation pulses: At 10179 cm^{-1} into

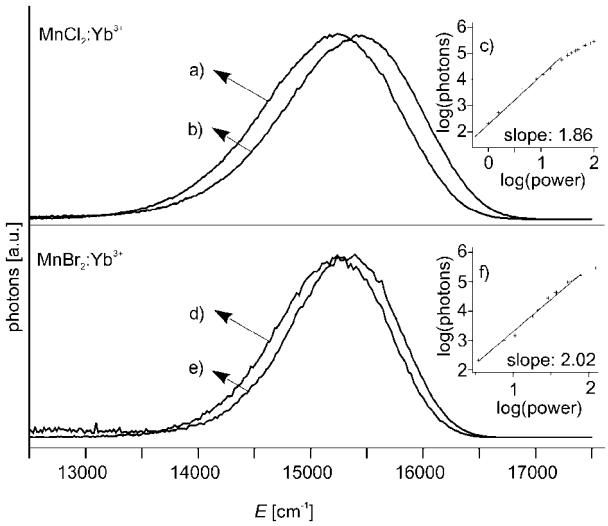

Figure 2. Mn^{2+} luminescence in $MnCl_2$:Yb^{3+} and $MnBr_2$:Yb^{3+} at 12 K after excitation into the respective Yb^{3+} excitations at 10765 cm^{-1} (a) and at 10675 cm^{-1} (d) and Mn^{2+} excitation at 21838 cm^{-1} in (b) and (e). The insets (c) and (f) show the corresponding power dependences of the Mn^{2+} emission intensity after Yb^{3+} excitation in the NIR in a double logarithmic representation.

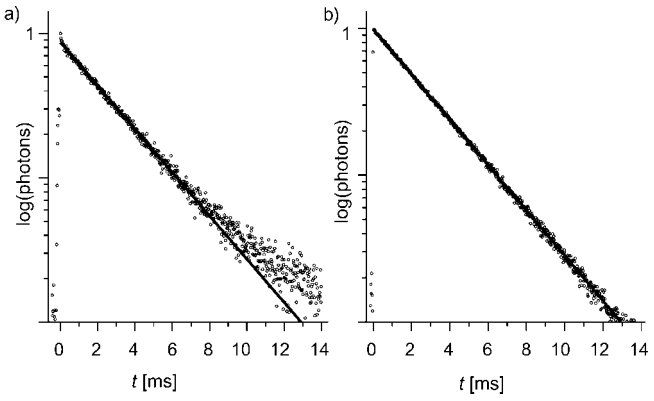

Figure 3. Temporal evolution in a semi-logarithmic representation of the Mn^{2+} emission intensity of $MnCl_2$:Yb^{3+} at 12 K after a 10 ns laser pulse at 10179 cm^{-1} (a) and at 18796 cm^{-1} (b). The full lines represent single-exponential fits to the non-logarithmic experimental data.

the Yb^{3+} $^2F_{5/2}$ (a) and at 18796 cm^{-1} into the Mn^{2+} $^4T_{1g}$ absorption (b). Both curves a) and b) can be fitted by single exponential decay functions with a lifetime $\tau = 2.8$ ms. The deviation from linearity at times above 10 ms in trace a) is an artefact close to the detection limit. For $MnBr_2$:Yb^{3+} at 12 K the Mn^{2+} $^4T_{1g}$ luminescence has a decay time $\tau =$ 1.4 ms after both Yb^{3+} and Mn^{2+} excitation (data not shown). At temperatures above 50 K the decay curves become increasingly non-single exponential with a fast and a slow component in both compounds. The lifetime of the Yb^{3+} $^2F_{5/2}$ luminescence at 12 K is $\tau = 2.2$ ms for $MnCl_2$:Yb^{3+} and $\tau = 1$ ms for $MnBr_2$:Yb^{3+} between 12 and 100 K.

Table 1. Comparison of the Mn^{2+}–Yb^{3+} bridging geometries, distances, Yb^{3+}-L-Mn^{2+} bridging angles and up-conversion efficiencies η_{UC} as defined in Equation (3) for various Mn^{2+}/Yb^{3+} UC systems. In all cases η_{UC} refers to a 191 mW laser beam focused onto the sample by an $f = 53$ mm lens.

Compound	Bridging geometry	Mn^{2+}–Yb^{3+} distance [Å]	Mn-L-Yb angle [°]	η_{UC} [%]	T [K]	Ref.
Rb_2MnCl_4:Yb^{3+}	corner	5.05	180	28 (site A)	35	[14]
Rb_2MnCl_4:Yb^{3+}	corner	5.05	180	18 (site B)	15	[14]
$CsMnCl_3$:Yb^{3+}	corner	5.20	177.2	8.5	75	[13]
$RbMnCl_3$:Yb^{3+}	**corner**/face	5.02	177.1	2	10	[12]
$MnCl_2$:Yb^{3+}	edge	3.71	92.8	4.1	12	this work
$MnBr_2$:Yb^{3+}	edge	3.82	89.8	1.2	12	this work
$RbMnCl_3$:Yb^{3+}	corner/**face**	3.20	77.9	0.02	10	[12]
$CsMnBr_3$:Yb^{3+}	face	3.26	74.8	0.05	12	[16]
$RbMnBr_3$:Yb^{3+}	face	3.37	76.1	0.05	12	[15]

Discussion

Yb^{3+}-Doped $MnCl_2$ and $MnBr_2$: $MnCl_2$ crystallizes in the layer-type $CdCl_2$ structure in the space group $R3m$ with the lattice constants $a = 3.711$ and $c = 17.566$ Å. The Mn^{2+} ions occupy slightly trigonally distorted octahedral sites. The $MnCl_6^{4-}$ units are arranged as layers of edge-sharing octahedra. The separation between two neighbouring Mn^{2+} ions within the layers is 3.71 Å. $MnBr_2$ has the layer-type CdI_2 structure and crystallizes in the space group $P3m1$ with the cell constants $a = 3.873$ and $c = 6.271$ Å. The nearest neighbour Mn^{2+}–Mn^{2+} distance within the layers is 3.82 Å. Both compounds are low-temperature antiferromagnets with Néel temperatures $T_N = 1.96$ and 2.16 K for $MnCl_2$[18] and $MnBr_2$,[19] respectively. Partial two-dimensional magnetic order is persistent to temperatures far above the Néel temperature.

The ionic radii of Mn^{2+} (0.83 Å) and Yb^{3+} (0.87 Å) are similar. Thus, Yb^{3+} is very likely to substitute for Mn^{2+} ions in $MnCl_2$ and $MnBr_2$, which makes charge compensation necessary. For compounds with linear chains of face-sharing octahedra, such as $CsCdBr_3$ for example, it has been shown that trivalent dopant ions preferentially occur in M^{3+}-vacancy-M^{3+} arrangements.[20] As in the other Yb^{3+} doped Mn^{2+} halide systems studied so far (see Table 1) an arrangement with a Mn^{2+} vacancy adjacent to two Yb^{3+} ions is also most likely for the Yb^{3+} dopant ions in $MnCl_2$ and $MnBr_2$. As a consequence, the $MnCl_2$ and $MnBr_2$ structures are distorted around the dopant ions.[12–14,16]

The sharp-line excitation and luminescence features in the NIR part of Figure 1 around 10000 cm^{-1} are due to Yb^{3+} $^2F_{7/2} \rightleftarrows {}^2F_{5/2}$ transitions. Both $^2F_{7/2}$ and $^2F_{5/2}$ are split by the crystal field. The most intense Yb^{3+} excitation lines at 10179 and 10765 cm^{-1} for $MnCl_2$:Yb^{3+} (see Figure 1) and at 10079 and 10675 cm^{-1} for $MnBr_2$:Yb^{3+}, respectively, are assigned to electronic origins. Below 100 K the Yb^{3+} $^2F_{5/2} \rightarrow {}^2F_{7/2}$ luminescence is radiative in low-phonon hosts like chlorides and bromides, due the large energy gap of around 10000 cm^{-1}.[21,22] The constancy of the Yb^{3+} luminescence intensity as well as the constant Yb^{3+} lifetime between 12 and 100 K in $MnCl_2$:Yb^{3+} and $MnBr_2$:Yb^{3+} substantiates this.

In $MnCl_2$:Yb^{3+} and $MnBr_2$:Yb^{3+} the broad red luminescence band is assigned to the Mn^{2+} $^4T_{1g} \rightarrow {}^6A_{1g}$ transition, see Figure 2 traces b) and e). At 150 K its intensity is reduced to less than 10% of the 12 K value for both $MnCl_2$:Yb^{3+} and $MnBr_2$:Yb^{3+}. This is attributed to the onset of efficient energy migration to killer traps within the Mn^{2+} system above 100 K[23] and an additional loss channel via the Yb^{3+} dopant ions at increased temperatures (see Figure 4 and next section).

For $MnCl_2$:Yb^{3+} the radiative lifetime of the Mn^{2+} $^4T_{1g}$ luminescence was estimated[21] from the $^4T_{1g}$ absorption intensity as $\tau_{rad} = 2.8$ ms, which is in perfect agreement with measured lifetime of $\tau = 2.8$ ms. This result indicates that the measured lifetime is in fact radiative at 12 K. In the case of $MnBr_2$:Yb^{3+} the estimated $\tau_{rad} = 1.9$ ms is about 30% longer than the experimental lifetime $\tau = 1.4$ ms at 12 K. This is attributed to a specifically high concentration of Mn^{3+} killer traps in MnBr:Yb^{3+} leading to non-radiative losses even at 12 K.

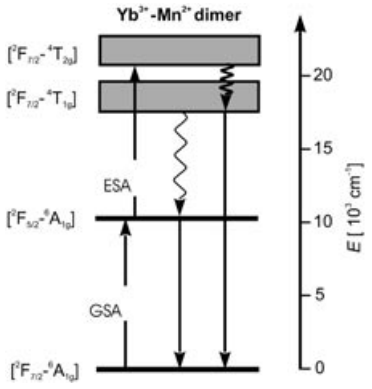

Figure 4. Schematic representation of the relevant upconversion mechanism in $MnCl_2$:Yb^{3+} and $MnBr_2$:Yb^{3+} using dimer notation. Straight and curly arrows denote radiative and non-radiative processes, respectively.

Upconversion mechanism in Yb^{3+} doped $MnCl_2$ and $MnBr_2$: The extremely weak green luminescence band III shown in Figure 1d is due to cooperative Yb^{3+} pair upconversion, which has been reported and studied for a variety of compounds.[16,24,25] The observation of this cooperative Yb^{3+} pair luminescence in this very lightly Yb^{3+}-doped system is an additional indication for the Yb^{3+} pair dopant arrangement in $MnCl_2$:Yb^{3+}.

As seen in Figure 2 the 12 K Mn^{2+} $^4T_{1g}\rightarrow{}^6A_{1g}$ luminescence is slightly red shifted when excited via Yb^{3+} in the NIR (traces a and d) compared with direct Mn^{2+} $^4T_{2g}$ excitation (traces b and e). This is indicative of different Mn^{2+} subsets emitting for the two excitations. Direct excitation into the Mn^{2+} $^6A_{1g}\rightarrow{}^4T_{2g}$ excites all Mn^{2+} ions of the crystal. At 12 K there is no extensive excitation energy migration within the $MnCl_2$ and $MnBr_2$ crystals.[26] As a consequence, luminescence will occur on the photoexcited Mn^{2+} ion or from one of its neighbours. At 100 K and above energy migration is extensive, and besides the intrinsic luminescence we observe luminescence from shallow traps and a part of the excitation is lost in deep traps. For Yb^{3+} excitation at 12 K we expect UC luminescence exclusively from Mn^{2+} ions adjacent to Yb^{3+}. The ligand field of these Mn^{2+} ions is slightly increased, due to a squeezing of the coordination by the near-by Yb^{3+} ion, and the luminescence is red-sifted.[27] The power dependence of the UC luminescence intensity with slopes of roughly 2 in the double logarithmic representation of Figure 2, insets, confirms the two-photon nature of the UC process.[28]

The excitation spectra in the Yb^{3+} absorption region monitoring the Mn^{2+} $^4T_{1g}\rightarrow{}^6A_{1g}$ UC luminescence and the Yb^{3+} $^2F_{5/2}\rightarrow{}^2F_{7/2}$ NIR luminescence (compare Figure 1c and a for $MnCl_2$:Yb^{3+}) are very similar in both title compounds. Therefore, we conclude that the Mn^{2+} UC luminescence is generated by Yb^{3+} absorption steps. This observation is remarkable, as the Yb^{3+} ion has no excited f–f states above 10000 cm^{-1} and the Mn^{2+} ion has no excited states below 18000 cm^{-1}. Therefore Yb^{3+} has not simply the role of a sensitizer, as it does in many lanthanide upconversion systems. In addition to being a sensitizer, it plays an active role in the upconversion process itself.

The temporal behaviour of an upconversion luminescence after short excitation pulses bears information on the nature of the underlying upconversion mechanism.[29] The transient in Figure 3a shows no rise of the Mn^{2+} $^4T_{1g}$ UC luminescence intensity in $MnCl_2$:Yb^{3+} at 12 K even at shortest times (640 ns) after the 10 ns excitation pulse. The same is true for the $MnBr_2$:Yb^{3+}. The data clearly bears the fingerprint of a sequential ground-state absorption (GSA) and excited-state absorption (ESA) mechanism, and a mechanism involving a slow energy transfer step can be ruled out.[29]

Both Yb^{3+} and Mn^{2+} are obviously involved in the process, and we use the most simple model of an exchange coupled Yb^{3+}–Mn^{2+} dimer to discuss the observed data. This is a gross simplification of the real situation, but nearest-neighbour interactions are the most important ones in an insulating magnet. The most relevant interaction is therefore included in the dimer model. In this picture exchange coupled Yb^{3+}–Mn^{2+} nearest neighbours act as the relevant chromophoric units. The GSA/ESA sequence proceeds as schematically shown in Figure 4, where the energy levels are denoted in Yb^{3+}–Mn^{2+} dimer notation. The GSA step excites the dimer from the [$^2F_{7/2}$-$^6A_{1g}$] ground state into the [$^2F_{5/2}$-$^6A_{1g}$] intermediate excited state, which is mainly localized on the Yb^{3+} ion. In the ESA step the dimer is promoted from the [$^2F_{5/2}$-$^6A_{1g}$] state into the Mn^{2+} centred [$^2F_{7/2}$-$^4T_{2g}$] upper excited state. Subsequent multiphonon relaxation processes (thick curly arrow) relax the dimer into the [$^2F_{7/2}$-$^4T_{1g}$] emitting state.

The same mechanism has also been successfully used to interpret similar phenomena in the cases of $RbMnCl_3$:Yb^{3+},[12] $CsMnBr_3$:Yb^{3+},[16] $RbMnBr_3$:Yb^{3+},[15] Rb_2MnCl_4:Yb^{3+}.[14] For $RbMnCl_3$:Yb^{3+} and $CsMnBr_3$:Yb^{3+} the ESA step was selectively probed in two-colour excited-state excitation spectra.[12,16]

Upconversion efficiency and the Yb^{3+}–Mn^{2+} bridging geometry: In our Yb^{3+}–Mn^{2+} systems the upconversion efficiency is experimentally accessible from the ratio of VIS/NIR emitted photons from the [$^2F_{7/2}$-$^4T_{1g}$] and [$^2F_{5/2}$-$^6A_{1g}$] states, as long as non-radiative relaxation from these states is negligible. For the Mn^{2+} halide systems in Table 1 this is valid only at temperatures below 100 K, the exact temperatures depending on the individual compound. It is appropriate to define the UC efficiency as:

$$\eta_{UC} = \frac{VIS_{em}}{NIR_{abs}} \quad (1)$$

Neglecting nonradiative losses at low temperatures we can approximate NIR_{abs} as follows

$$NIR_{abs} \cong NIR_{em} + 2 \times VIS_{em} \quad (2)$$

and we obtain

$$\eta_{UC} \cong \frac{VIS_{em}}{NIR_{em} + 2 \times VIS_{em}} \quad (3)$$

The experimental photon ratio as given in Equation (3) can be used as a reasonable measure for the efficiency of our

UC process at low temperatures. According to this definition the theoretical upper limit of the upconversion efficiency η_{UC} is 0.5. This corresponds to the situation where all absorbed NIR photons are upconverted into VIS photons. For the most efficient site A of $Rb_2MnCl_4:Yb^{3+}$ at 35 K under the excitation conditions of Table 1 this means that 56% of the absorbed NIR photons are upconverted, which is a very high number for an upconversion process. Owing to the non-linear nature of upconversion processes the η_{UC} values in Table 1 are dependent on the excitation conditions.[28] All given η_{UC} values correspond to excitation at 191 mW focused onto the sample by a 53 mm focal lens.

From Table 1 it appears evident that the bridging geometry between Yb^{3+} and Mn^{2+} octahedra is a determinant parameter for the upconversion efficiency. Along the series from purely corner-sharing bridging in $Rb_2MnCl_4:Yb^{3+}$ to edge-sharing in $MnCl_2:Yb^{3+}/MnBr_2:Yb^{3+}$ to face-sharing connectivity in $CsMnBr_3:Yb^{3+}$ the observed UC efficiency decreases by three orders of magnitude from astounding 28% to 0.05%. The relevant Yb^{3+}–Mn^{2+} dimer units of this series are depicted in Figure 5. The nearest neighbour distance between Yb^{3+} and Mn^{2+} ions decreases from 5.05 Å in the corner-sharing case to 3.71 Å in the edge-sharing and 3.26 Å in the face-sharing case. Both $MnCl_2:Yb^{3+}$ and $MnBr_2:Yb^{3+}$ exclusively allow an edge-sharing arrangement of the active ions. The UC efficiencies between the chloride and the bromide differ by approximately a factor 3, as seen in Table 1. This reduction is much smaller than the differences in UC efficiency between the bridging geometries. This indicates that the nature of the halide ion is not the determining factor for the upconversion efficiency.

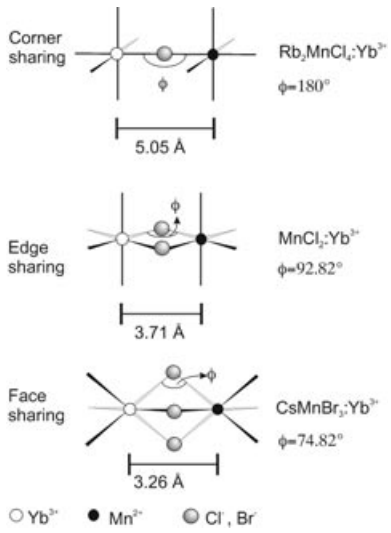

Figure 5. Bridging geometries between adjacent octahedra in Yb^{3+} doped Mn^{2+} halide compounds.

The observed decreasing efficiency with decreasing distance between the active ions clearly eliminates electric multipole–multipole interactions as being responsible for the UC process. It strongly indicates that super-exchange interactions, which are not only distance dependent but also strongly geometry dependent, are responsible for our observed effects.

In 1966 Tanabe and co-workers[30] developed a formalism to account for the enhancement of spin-forbidden transitions in magnetically coupled transition metal ion compounds. Since then it has been applied to a wide variety of magnetically coupled transition metal spin clusters and magnetically ordered materials with good results.[31–34] A relevant example for our discussion are the unusual transitions in Cr^{3+} doped $EuAlO_3$ crystals, which have been explained on the basis of this model.[35] Besides the normal R lines corresponding to Cr^{3+} $^2E \rightarrow {}^4A_2$ transitions, prominent red-shifted lines were found in the luminescence spectrum. The authors of reference[35] convincingly showed that in the final state of these transitions the Eu^{3+} ions are not in the $^7F_0$ ground state but in excited ^7F_J states. This example is evidently analogous to our case: an excitation on one ion is coupled to a de-excitation of the partner, which corresponds to the ESA step in Figure 4. A dimer model of exchange-coupled ions appears to be perfectly appropriate to account for such effects, even in situations which are physically more complicated. According to Tanabe et al. the interaction which leads to this spin-dependent intensity can be formulated as follows for an exchange coupled dimer:[30]

$$\hat{H} = \sum_{i,j} (\Pi_{a_i b_i} \cdot \vec{E})(\vec{s}_{a_i} \cdot \vec{s}_{b_i}) \tag{4}$$

In Equation (4), i and j refer to the unpaired electrons situated in orbitals on the two magnetic ions a and b, respectively. $\vec{E}$ is the electric vector of the light. It was shown in reference [30] that the components can be related to the orbital parameters constituting the ground-state exchange parameter:

$$\Pi_{a_i b_j} = \left(\frac{\partial J_{a_i b_j}}{\partial E}\right) E \rightarrow 0 \tag{5}$$

where

$$J = \frac{1}{n_a \cdot n_b} \sum_{i,j} J_{a_i b_j} \tag{6}$$

Very reasonable estimates of the parameters can be obtained for transition metal systems from quantum-chemical calculations.[36] In the theory of kinetic exchange $J_{a_i b_j}$ derives from an electron transfer:[37,38]

$$J_{a_i b_j} = \frac{2|\langle b_j|\hat{h}|a_i\rangle|^2}{U} \tag{7}$$

In Equation (7), $\hat{h}$ is a one-electron Hamiltonian, and the transfer integral in the numerator corresponds to the resonance integral in MO theory and can be calculated.[36] U is the energy of the excited state in which one electron is transferred from a_i to b_j or vice versa.

In our Yb^{3+}–Mn^{2+} dimer there is one unpaired electron on Yb^{3+} and there are five unpaired electrons in the ground state of Mn^{2+}, we thus have five terms in the sums of Equa-

tions (4) and (5). For an estimate of their strengths we have to consider the specific bridging geometry between Yb^{3+} and Mn^{2+} in a given lattice.

For the corner-sharing situation with $\phi = 180°$ in Figure 5 we can use this formalism to qualitatively rationalize the high UC efficiencies observed in these systems. The transfer integral $\langle b_j|\hat{h}|a_i\rangle$ can be taken to be proportional to the overlap integral $\langle b_j|a_i\rangle$.[39] In Figure 6 we draw schematic pictures of the two most relevant overlap pathways of unpaired electron orbitals via the intervening occupied ligand orbitals. In this geometrical arrangement the unpaired electron on the Yb^{3+} is residing in the f_{z^3} orbital, which is assumed to be the least stable of all the 4f orbitals as it is pointing straight towards the ligand p_z orbital. It will overlap with both s and p_z ligand orbitals, thus transferring some Yb^{3+} spin density onto the bridge. On the Mn^{2+} side all five 3d orbitals are singly occupied, and all the five orbital $J_{f_z^3,b_j}$ exchange parameters will have non-zero values. But the dominant one will undoubtedly be $J_{f_z^3,d_z^2}$. It will be antiferromagnetic and have contributions from both pathways in Figure 6. Thus, by way of Equation (5) $\Pi_{f_z^3,d_z^2}$ will be the dominant factor in the expression for exchange-induced intensity. The situation shown in Figure 6 corresponds to the best possible overlap of the magnetic orbitals on Yb^{3+} and Mn^{2+}. For smaller bridging angles than $\phi = 180°$ the overlap and transfer integrals through the ligand p orbitals are reduced. With this simple picture we can thus rationalize that the highest UC efficiencies are observed for linear Yb^{3+}-Cl-Mn^{2+} arrangements. We cannot, however, quantitatively reproduce the observed reductions. Thus, there is more predictive power in the empirical correlation of optical and structural properties in Table 1 itself than in any orbital model.

Attempts have been made to rationalize our observed correlations by using DFT methods to calculate the transfer integrals for the various geometries. No conclusive results were obtained, however, which was mainly ascribed to the poor quality of the available DFT basis sets for Yb^{3+}. Atanasov et al. formulated a procedure for the calculation of the relevant transfer integrals and J parameters in the ground and excited states for rare earth/transition metal dimers.[40] First results point to the possibility that for certain angles also the potential exchange has significant contributions. Further work is clearly needed for a better understanding of the exchange coupling in rare earth/transition metal systems, and this might then lead to a more quantitative understanding for our observed optical/structural correlations.

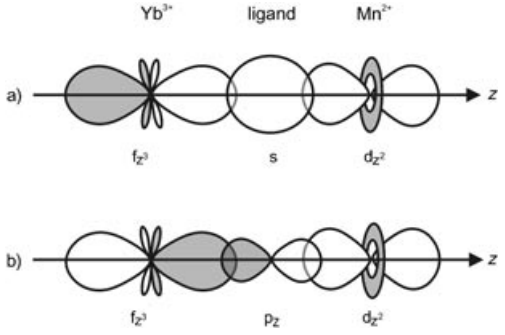

Figure 6. Schematic representation of the most important sigma overlaps between singly occupied metal and fully occupied ligand orbitals for a bridging angle ϕ of 180°.

Conclusions

Yb^{3+} containing Mn^{2+} halide compounds show a cooperative upconversion process involving both the rare earth and the transition metal ion. On the basis of an exchange coupled Yb^{3+}–Mn^{2+} dimer model, it is possible to account for the experimental data. The systematic study of the influence of the connectivity between Yb^{3+} and Mn^{2+} octahedra on the upconversion properties reveals a strong dependence of the UC efficiency on the Yb^{3+}-L-Mn^{2+} ($L = Cl^-$, Br^-) bridging angle. The bridging geometry which opens an efficient exchange pathway is more important than the distance between the metal ions or the nature of the bridging halide ligands. The example of Rb_2MnCl_4:Yb^{3+} shows that exchange interactions between rare earth and transition metal ions can induce very efficient cooperative upconversion processes at low temperatures. However, in all the Yb^{3+} doped Mn^{2+} halides listed in Table 1 the UC luminescence is quenched at temperatures above 150 K. This is due, on the one hand, to killer traps such as Mn^{3+}, which capture the excitation at higher temperatures. On the other hand, there is a nonradiative loss process depicted by a light curly arrow in Figure 4, which depopulates the $^4T_{1g}$ state. This latter process is intrinsic to Yb^{3+}/Mn^{2+} systems, and there is no obvious way to get around it by engineering a new material. One way to improve the situation at higher temperatures is to go to Mn^{2+} in tetrahedral coordination. We have recently for the first time observed Mn^{2+} UC luminescence at room temperature in Yb^{3+} and Mn^{2+} co-doped Zn_2SiO_4, $CaZnF_4$ and $SrZnCl_4$.[41,42]

Experimental Section

Crystal growth and manipulation: Single crystals of Yb^{3+}-doped $MnCl_2$ and $MnBr_2$ were grown by the Bridgman technique from polycrystalline $MnCl_2$ and $MnBr_2$ with addition of 1 mol% $YbCl_3$ and $YbBr_3$, respectively. $MnCl_2$ (Aldrich, 99.999%) was used without further purification. $MnBr_2$ (CEREAC, 99.5%) was used after sublimation at 700°C. $YbCl_3$ and $YbBr_3$ were prepared from Yb_2O_3 (Ultra-Function Enterprise Co Ltd, 99.9999%), NH_4X X = Cl, Br (Merck, p.a., sublimed), and HCl (30%, Merck, suprapur) using the NH_4Cl method.[43] The effective Yb^{3+} concentration in $MnCl_2$ and $MnBr_2$ was 0.1 ± 0.01 mol% and 0.06 ± 0.01 mol%, respectively and was measured by ICP-OES. Plate like crystals with faces perpendicular to the c axis and good optical quality were obtained and checked by X-ray powder diffraction. All spectroscopic measurements were conducted on crystals very smooth surfaces under the optical microscope and dimensions between $5 \times 3 \times 1$ mm^3 and $10 \times 4 \times 2$ mm^3. Both the starting materials and the crystals are hygroscopic; therefore all the handling was carried out in a glove box under N_2 atmosphere. For the experiments crystals where mounted in a sealed copper cell or in closed quartz glass ampoules with He atmosphere.

Spectroscopic measurements: Sample cooling for absorption measurements was achieved using a closed cycle cryostat (Air Products). The He flow tube technique was used for luminescence experiments. Absorption spectra were measured on a Cary 5E (Varian) spectrometer. Upcon-

version was excited with an Nd^{3+}:YVO_4 laser (Spectra Physics Millennia Xs) pumped tuneable Ti:sapphire laser (Spectra Physics 3900S). Wavelength control was achieved by an inchworm driven (Burleigh PZ-501) birefringent filter and a wavemeter (Burleigh WA2100). The sample luminescence was dispersed by a 0.85 m double monochromator (Spex 1402) with 500 nm blazed 1200 groves mm^{-1} gratings. VIS and NIR luminescences were detected by a cooled photomultiplier tube (Hamamatsu 3310-01) in connection with a photon-counting system (Stanford Research SR 400). Mn^{2+} downconversion luminescence was excited by the 457.9 nm line of the Ar^+ ion laser and detected as described above. The excitation laser beam was focused on the sample with an $f=53$ mm focal lens. All spectra are corrected for the wavelength dependence of the sensitivity of the monochromator and detection system (measured with a calibrated 60 W tungsten lamp (2900 K) as black body radiation source) and for the refractive index of air (vacuum correction). The spectra are presented as number of photons versus wavenumber. All excitation scans were corrected for the power dependence of the Ti:sapphire laser source over the tuning range. The laser power was measured with a power meter (Coherent Labmaster-E).

For time resolved measurements 10 ns pulses of the second harmonic of a Nd^{3+}/YAG (Quanta Ray DC R 3) pumped dye laser (Lambda Physik FL3002; Pyridine 1 in methanol) was Raman shifted (Quanta Ray, RS-1, H_2, 340 psi, operative range 935–1025 nm). Square wave pulses in the same spectral range were generated with an acousto-optic modulator (Coherent 305) controlled by a function generator (Stanford Research Systems DS345). For these pulsed experiments the sample luminescence was dispersed by a 0.75 m single monochromator (Spex 1702) equipped with a 750 nm blazed 600 grooves mm^{-1} grating and detected with a photomultiplier (Hamamatsu 3310-01) and a multi-channel scaler (Standford Research SR430).

All emission and excitation spectra as well as the pulsed experiments were measured in a 90° arrangement between incoming laser beam and the luminescence detection system used.

Acknowledgements

The Swiss National Science Foundation and the Portland Cement Foundation financially supported this work. The authors are grateful to Claude Daul, Michael Atanasov and Pio Bättig for fruitful discussions about the theoretical description of the Yb^{3+}–Mn^{2+} exchange interactions.

[1] E. Downing, L. Hesselink, J. Raltson, R. Macfarlane, *Science* **1996**, *273*, 1185.
[2] F. Auzel, *Chem. Rev.* **2004**, *104*, 139–173, and references therein.
[3] O. S. Wenger, H. U. Güdel, *Inorg. Chem.* **2001**, *40*, 157–164.
[4] M. Wermuth, H. U. Güdel, *J. Lumin.* **2000**, *87–89*, 1014–1016.
[5] D. R. Gamelin, H. U. Güdel, *J. Phys. Chem. B* **2000**, *104*, 11045.
[6] F. Auzel, *F. C. R. Acad. Sci. (Paris)* **1966**, *262*, 1016.
[7] W. Lenth, R. Macfarlane, *Opt. Photonics News* **1992**, *3*, 8.
[8] A. Aebischer, O. S. Wenger, H. U. Güdel, *J. Lumin.* **2003**, *102–103*, 48–53.
[9] C. Reinhard, K. Kramer, D. A. Biner, H. U. Güdel, *J. Chem. Phys.* **2004**, *120*, 3374–3380.
[10] P. Gerner, K. Krämer, H. U. Güdel, *J. Lumin.* **2003**, *102–103*, 112–118.
[11] S. Heer, M. Wermuth, K. Kramer, H. U. Güdel, *Chem. Phys. Lett.* **2001**, *334*, 293–297.
[12] R. Valiente, O. S. Wenger, H. U. Güdel, *Phys. Rev. B* **2001**, *63*, 165102.
[13] R. Valiente, O. S. Wenger, H. U. Güdel, *J. Chem. Phys.* **2002**, *116*, 5196.
[14] C. Reinhard, R. Valiente, H. U. Güdel, *J. Phys. Chem. B* **2002**, *106*, 10051.
[15] P. Gerner, Diploma Thesis, University of Bern, **2000**.
[16] P. Gerner, O. S. Wenger, R. Valiente, H. U. Güdel, *Inorg. Chem.* **2001**, *40*, 4534.
[17] H. J. W. M. Hoekstra, C. Haas, *Phys. B* **1985**, *138*, 327–336.
[18] M. Regis, Y. Farge, *J. Phys.* **1976**, *37*, 627–636.
[19] E. O. Wollan, W. C. Koehler, M. K. Wilkinson, *Phys. Rev.* **1958**, *110*, 638–646.
[20] G. L. McPherson, L. M. Henling, *Phys. Rev. B* **1977**, *16*, 1889–1892.
[21] T. C. Brunold, H. U. Güdel, *Luminescence Spectroscopy, in Inorganic Electronic Stucture and Spectroscopy* (Eds.: E. I. Solomon, A. B. P. Lever), Wiley, New York, **1999**, pp. 259–306.
[22] G. F. Imbusch, R. Kopelman, *Optical Spectroscopy of Electronic Centers in Solids, in Laser Spectroscopy of solids* (Eds.: W. M. Yen, P. M. Selzer), Springer, Berlin, **1981**, p. 3.
[23] G. L. McPherson, K. Talluto, R. A. Auerbach, *Solid State Commun.* **1982**, *43*, 817–819.
[24] P. Goldner, F. Pelle, F. Auzel, *J. Lumin.* **1997**, *72–74*, 901–903.
[25] M. P. Hehlen, H. U. Güdel, *J. Chem. Phys.* **1993**, *98*, 1768–1775.
[26] C. R. Ronda, H. H. Siekman, C. Haas, *Physica B+C* **1987**, *144*, 331–340.
[27] R. D. Shannon, *Acta Crystallogr. Sect. A* **1976**, *32*, 751–767.
[28] M. Pollnau, D. R. Gamelin, S. R. Lüthi, M. P. Hehlen, H. U. Güdel, *Phys. Rev. B* **2000**, *61*, 3337–3346.
[29] D. R. Gamelin, H. U. Güdel, *Top. Curr. Chem.* **2001**, *214*, 1–56.
[30] J. Ferguson, H. J. Guggenheim, Y. Tanabe, *J. Phys. Soc. Jpn.* **1966**, *21*, 692–704.
[31] I. Tsujikawa, *J. Phys. Soc. Jpn.* **1963**, *18*, 1391–1399.
[32] T. Fujiwara, *J. Phys. Soc. Jpn.* **1973**, *34*, 1180–1191.
[33] J. Van der Ziel, *J. Chem. Phys.* **1972**, *57*, 2442–2450.
[34] H. J. W. M. Hoekstra, C. R. Ronda, C. Haas, *Physica B+C* **1983**, *122*, 295–301.
[35] J. P. van der Ziel, L. G. van Uitert, *Phys. Rev.* **1969**, *180*, 343–349.
[36] P. J. Hay, J. C. Thibeault, R. Hoffmann, *J. Am. Chem. Soc.* **1975**, *97*, 4884–4899.
[37] H. Weihe, H. U. Güdel, *Inorg. Chem.* **1997**, *36*, 3632–3639.
[38] H. Weihe, H. U. Güdel, *J. Am. Chem. Soc.* **1997**, *119*, 6539–6543.
[39] H. B. Gray, C. J. Ballhausen, *J. Am. Chem. Soc.* **1963**, *85*, 260–265.
[40] M. Atanasov, C. A. Daul, H. U. Güdel, *Modelling of Anisotropic Exchange Coupling in Rare-Earth/Transition Metal Pairs: Applications to Yb^{3+}–Mn^{2+} and Yb^{3+}-Cr^{3+} halide Clusters and its Implication to the Light Upconversion*, in *Computational Chemistry: Reviews of Current Trends* (Eds: J. Leszczynski), World Scientific, Singapore, **2004**, in press.
[41] P. Gerner, C. Fuhrer, C. Reinhard, H. U. Güdel, *J. Alloys Compd.* **2004**, in press.
[42] C. Reinhard, P. Gerner, F. Rodriguez, S. Garcia-Revilla, R. Valiente, H. U. Güdel, *Chem. Phys. Lett.* **2004**, *386*, 132–136.
[43] G. Meyer, *Inorg. Synth.* **1989**, *25*, 146–150.

Received: March 23, 2004
Published online: August 11, 2004

